

NANO EXPRESS

Open Access



RNA m⁶A Alterations Induced by Biomineralization Nanoparticles: A Proof-of-Concept Study of Epitranscriptomics for Nanotoxicity Evaluation

Jinbin Pan^{1*†}, Jiaojiao Wang^{3†}, Kun Fang^{4†}, Wenjing Hou⁵, Bing Li², Jie Zhao^{2*} and Xinlong Ma^{2*}

Abstract

Although various strategies have been included in nanotoxicity evaluation, epitranscriptomics has rarely been integrated into this field. In this proof-of-concept study, N⁶-methyladenosine (m⁶A) changes of mRNA in HEK293T cells induced by three bovine serum albumin (BSA)-templated Au, CuS and Gd₂O₃ nanoparticles are systematically explored, and their possible biological mechanisms are preliminarily investigated. It has been found that all the three BSA-templated nanoparticles can reduce m⁶A levels, and the genes with reduced m⁶A are enriched for TGF-β signaling, which is critical for cell proliferation, differentiation and apoptosis. Further results indicate that abnormal aggregation of m⁶A-related enzymes at least partly account for the nanoparticle-induced epitranscriptomic changes. These findings demonstrate that epitranscriptomics analysis can provide an unprecedented landscape of the biological effect induced by nanomaterials, which should be involved in the nanotoxicity evaluation to promote the potential clinical translation of nanomaterials.

Keywords: Epitranscriptomics, Nanotoxicity, RNA N⁶-methyladenosine, Nanomaterials, Biomineralization

Introduction

Nanosafety is attracting considerable attention with the booming development and extensive applications of nanotechnology in the field of biomedicine [1, 2]. Although versatile nanomaterials with unique physicochemical characteristics are promising for diagnosis and therapy of diverse diseases, few nanoagents have been approved for clinical use due to the indistinct biosafety [3]. As a result, a standard and comprehensive

nanotoxicological evaluation framework is highly desired for clarifying biosafety of nanoagents to guide their controlled synthesis and promote their clinical translation [4–6].

In the past decade, various strategies have been developed to evaluate nanotoxicity from in vitro to in vivo (Fig. 1a) [7–18], and the adverse outcome pathway (AOP) framework and the quantitative structure–activity relationship (QSAR) modeling have been commonly used at the cellular level due to their simplified process, high efficiency, good logicity and predictability [8, 19–21]. However, these methods generally focus on specific genes, proteins, organelles and biological processes, which cannot provide a full picture of the nano-biological interactions [7]. In contrast, the emerging omics analysis can provide full characterization and quantification of biological effects of nanomaterials at a given molecular level, such as DNA, RNA, proteins, and lipids [22]. By

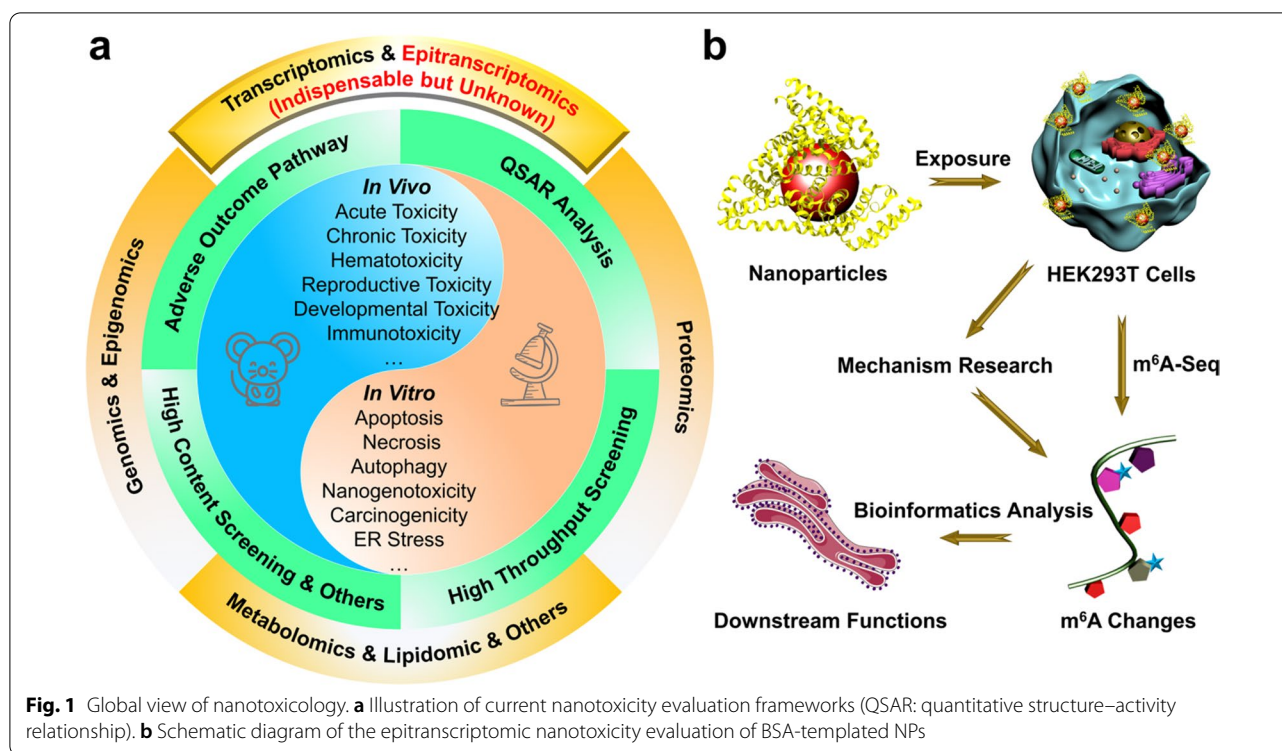
*Correspondence: panjinbin@tmu.edu.cn; zhaojie@tmu.edu.cn; maxinlong8686@yeah.net

[†]Jinbin Pan, Jiaojiao Wang, and Kun Fang have contributed equally to this work.

¹ Department of Radiology, Tianjin Key Laboratory of Functional Imaging, Tianjin Medical University General Hospital, Tianjin 300052, China

² Department of Orthopedics, Tianjin Hospital, Tianjin University, Tianjin 300211, China

Full list of author information is available at the end of the article



integrating with bioinformatic analysis, the omics-based approaches are capable of mapping the toxicity-related molecular pathways and biological processes [23]. To date, nanotoxicology has entered into a new era following the development of various omics-based methods, such as genomics [24], epigenomics [25], transcriptomics [26, 27], proteomics [28], lipidomics [29, 30], and metabolomics [22, 31, 32].

Epitranscriptomics describes post-transcriptional RNA modifications that can dynamically regulate gene expression and control cell fate [33]. N⁶-methyladenosine (m⁶A) is the most abundant internal mRNA modification in eukaryotic cells, which functionally modulates the eukaryotic transcriptome to influence mRNA splicing, export, localization, translation and stability [34–37], as well as to regulate the expression of genes controlling extensive biological processes, such as development, reproduction, metabolism, immunity, and tumorigenesis [34, 38, 39]. Aberrant m⁶A as crucial drivers of multiple diseases (especially cancers) can provide an epitranscriptomic indicator of cellular responses and pathogenetic effects induced by nanomaterials, of which field remains largely unknown [40–43]. Although several omics-based approaches have been used to assess biological effects of nanomaterials, the epitranscriptomics has rarely been applied in the field of nanosafety evaluations so far [44]. Therefore, it is of great significance to investigate the nanomaterial-induced epitranscriptomics scenery.

Protein-templated biomineralization nanomaterials have attracted considerable interests in the field of biomedicine, and shown great potential in clinical translations due to their facile synthesis process, ultra-small and uniform size, remarkable colloidal stability and water solubility, good biocompatibility and favorable theranostics capability [45, 46]. In this proof-of-concept study, three types of bovine serum albumin (BSA)-templated nanoparticles (NPs) for different biological applications (BSA-Au NPs for fluorescent imaging, BSA-CuS NPs for photothermal therapy, and BSA-Gd₂O₃ NPs for magnetic resonance imaging) were employed to study the nanotoxicity in terms of epitranscriptomics. These NPs were synthesized by the biomineralization method, and m⁶A changes induced by these NPs were measured by the immunoprecipitation sequencing (m⁶A-seq). Functional annotation of genes with m⁶A changes were performed using the bioinformatic analysis, and biological mechanisms accounting for m⁶A changes were investigated via cell biological techniques (Fig. 1b). These results indicated that BSA-templated NPs could interfere the processing of m⁶A-related enzymes to reduce m⁶A level of diverse genes, which are relevant to multiple cellular pathways and biological processes. Therefore, epitranscriptomic effects (e.g., the m⁶A changes) induced by NPs were nonnegligible biological events, which should be integrated into the biosafety evaluation of nanomaterials for their potential clinical translation.

Experimental

Synthesis of BSA-Templated NPs

For the synthesis of BSA-Au NPs, 2 mL of aqueous HAuCl_4 solution (25 mM, 37 °C) was added to 8 mL of BSA solution (250 mg, 37 °C) under vigorous stirring. Five minutes later, 0.5 mL of NaOH solution (1 M) was added, and the reaction was kept under vigorous stirring at 37 °C for 12 h.

For the synthesis of BSA-CuS NPs, 1 mL of aqueous $\text{Cu}(\text{NO}_3)_2$ solution (200 mM) was added to 7.5 mL of BSA solution (250 mg) under vigorous stirring. Five minutes later, 0.5 mL of NaOH solution (1 M) was quickly added. Then, 2 mL of Na_2S (200 mM) was added and the reaction was kept under vigorous stirring at 90 °C for 0.5 h.

For the synthesis of BSA- Gd_2O_3 NPs, 0.5 mL of aqueous $\text{Gd}(\text{NO}_3)_3$ solution (100 mM) was added to 9.5 mL of BSA solution (250 mg) under vigorous stirring. Five minutes later, 0.5 mL of NaOH solution (1 M) was added, and the reaction was kept under vigorous stirring at room temperature for 2 h.

All these obtained BSA-templated NPs were purified by dialysis (molecular weight cut off: 8–14 kDa), and then freeze-dried and stored in dark at 4 °C for further use.

Characterization of NPs

The size and morphology of BSA-templated NPs were determined on a Philips Tecnai G^2 F20 (Philips, Holland) field emission transmission electron microscopy (TEM). The Fourier transform infrared (FT-IR) spectra (650 – 4000 cm^{-1}) of BSA, BSA-Au, BSA-CuS, and BSA- Gd_2O_3 NPs were measured on a Nicolet iS10 spectrometer (Nicolet, USA) with background of pure KBr. Fluorescent spectra were recorded on a F7000 spectrofluorometer (Hitachi, Japan) equipped with a plotter unit and a quartz cell (1 cm \times 1 cm). The absorption spectra were obtained via a UV-3600 plus spectrophotometer (Hitachi, Japan). The hydrodynamic size and zeta potential were determined on a Malvern Zetasizer (Nano series ZS, UK). The metal elements in nanoparticles were identified through the inductively coupled plasma-atomic emission spectrometer (ICP-AES, Thermo Fisher, ICAP 7400, USA).

Storage Stability of NPs

To investigate the storage stability of BSA-templated metallic nanoparticles, the three NPs in freeze-dried powder state and aqueous state (4 mg/mL) were stored at 4 °C for 2 weeks, and their common state, optical absorption property, fluorescence property, magnetic resonance imaging capability, and hydrodynamic size were

systematically evaluated at different timepoints (0, 7, and 14 days).

Protein Corona Analysis

We preliminarily evaluated the protein corona formation in vitro by mixing the BSA-templated NPs (5 mg/mL) with 10% fetal bovine serum (FBS). Then, the mixing solutions were put into an oscillator under 37 °C, and the hydrodynamic sizes of solutions were monitored at different timepoints (0, 0.5, 1, and 3 h) post-mixing.

Plasmids

The pFLAG-CMV vectors were provided by Sigma. Human METTL3 was cloned into pFLAG-CMV vectors by Gibson clone with forward primer ACAAGCTTG CGG CCGCGAATTCAatgtcggacacgtggag and reverse primer GGTCACAGGGATGCCACCCG GGATCC taattcttaggttagag.

Cell Culture and Transfection

HEK293T cells were obtained from American Type Culture Collection (ATCC) and grown in DMEM medium (Invitrogen) containing 10% FBS and 1% penicillin–streptomycin. Plasmids were transfected into cells with Lipofectamine 3000 (Invitrogen) according to manufacturer's instructions.

Cytotoxicity of NPs

The cytotoxicity of BSA-templated NPs was measured with HEK293T cells and 3T3-L1 cells via the standard Methyl Thiazolyl Tetrazolium (MTT) assays. Cells were seeded in 96-well culture plates at density of 1×10^4 cells/well in 2 mL of DMEM supplemented with 10% FBS and 1% penicillin–streptomycin at 37 °C under 5% CO_2 and cultured for 24 h. Then, the stale medium in each well was replaced with 2 mL of fresh medium containing different concentrations (50, 100, and 200 $\mu\text{g}/\text{mL}$) of NPs (BSA-Au, BSA-CuS, and BSA- Gd_2O_3 NPs), respectively. After another 24-h incubation, the cells were washed with PBS and treated with fresh medium containing MTT (0.25 mg/mL). Four hours later, the supernatant in each well was replaced with 120 μL of DMSO. After a mild shake for 10 min, the absorbance of each well at 490 nm was measured on a microplate reader (Bio-tek, USA). Then, the cell viability under the exposure of BSA-templated NPs was calculated.

To evaluate the influences of NPs on the apoptosis of cells, HEK293T cells were incubated in six-well culture plates at a density of 1×10^5 cells per well in 200 μL of DMEM supplemented with 10% FBS and 1% penicillin–streptomycin at 37 °C under 5% CO_2 and cultured for 24 h. Then, the stale medium in each well was replaced with 200 μL of fresh medium containing different

concentrations (50, 100, and 200 $\mu\text{g}/\text{mL}$) of NPs (BSA-Au, BSA-CuS, and BSA-Gd₂O₃ NPs), respectively. After incubation for another 24 h, the apoptosis of HEK293T cells was evaluated by using Annexin V-FITC/PI Apoptosis Detection Kit (KeyGEN, Shanghai, China).

Nanoparticles Uptaken by Cells

The nanoparticles uptake rates by HEK293T cells were identified through the ICP-AES. Briefly, HEK293T cells were seeded in a 10 cm-culture dish at a density of 1×10^6 cells/dish in 8 mL of DMEM supplemented with 10% FBS and 1% penicillin–streptomycin at 37 °C under 5% CO₂, and cultured for 24 h. Then, 8 mL of fresh culture medium containing 200 $\mu\text{g}/\text{mL}$ nanoparticles (BSA-Au, BSA-Gd₂O₃, and BSA-CuS NPs) was used to replace the old culture medium in each dish. After another 24-h incubation, the cells were washed with PBS, digested from the dish bottom with trypsin, and dispersed in PBS. After centrifugation at 1000 rpm for 3 min, and the supernatant was discarded. This washing process was repeated 3 times. Finally, these cells were fully dissolved with aqua regia, and the metal elements were quantified by ICP-AES. Cells cultured with 8 mL of fresh medium without nanoparticles were processed in the same way as the control group.

m⁶A-seq and Data Analysis

m⁶A-seq was performed following previously reported protocol [47]. Total RNA was extracted by homogenizing cells in TRIzol reagent. mRNA was further purified using GenElute™ mRNA Miniprep Kit (Sigma). RNA fragmentation and m⁶A-immunoprecipitation were performed with Magna MeRIP™ m⁶A Kit according to the instructions. The library preparation and sequencing were carried out on Illumina HiSeq 2000 according to the manufacturer's instructions. Samples were sequenced by with single-end 50-bp read length. All reads were mapped to human genome version hg19 by tophat v2.0.13 with default settings. The m⁶A level changes for nanoparticles/control were calculated by using exomePeak. Gene expression level changes for input and treatment were analyzed using Cuffdiff. The sequence reads were visualized with Integrative Genomics Viewer [48].

Redox-Western Blotting

Cells were lysed using high KCl lysis buffer and sonicated [49]. Equal amounts of proteins were loaded and separated by SDS-PAGE, transferred to polyvinylidene fluoride membranes, and detected by immunoblotting with the Millipore Immobilon Western Chemiluminescent HRP Substrate. Antibodies used for western blotting were as follows unless otherwise specified: METTL3, METTL14, WTAP, and FTO were bought from Cell

Signaling Technology (CST), ALKBH5, YTHDC1, YTHDF2, and YTHDF3 were obtained from (Protein-Tech), and FLAG (M2, F3165) was provided by Sigma-Aldrich. β -actin and β -tubulin (Santa Cruz) were used as loading controls.

RNA Isolation and Quantitative RT-PCR

Total RNA was isolated from cultured cells using TRIzol reagent. First-strand complementary DNA (cDNA) was synthesized by reverse transcription of 1 μg RNA using HiScript Q RT SuperMix for qPCR (+gDNA wiper) (Vazyme). QPCR was carried out using ChamQ Universal SYBR qPCR Master Mix (Vazyme) and mRNA expressions were normalized to reference genes GAPDH. The primers used in all qPCR assays are listed in Additional file 1: Table S1 [50, 51].

MeRIP-qPCR

The MeRIP-qPCR was conducted as previously reported [52]. Briefly, total RNA was isolated with Trizol reagent, and then mRNA was further purified using GenElute™ mRNA Miniprep Kit (Sigma). Two μg of the purified mRNA was fragmented into 100–200 nt length with fragmentation buffer at 94 °C for 5 min. The mRNA fragments were purified with Rneasy Mini Kit (QiaGen) and then subjected to immunoprecipitation with m⁶A antibody. After extensive wash, the immunoprecipitated fragments were eluted by competition using free N⁶-methyladenosine and then used for cDNA construction and qPCR analysis. The primers used in m⁶A-qPCR assays are listed in Additional file 1: Table S2.

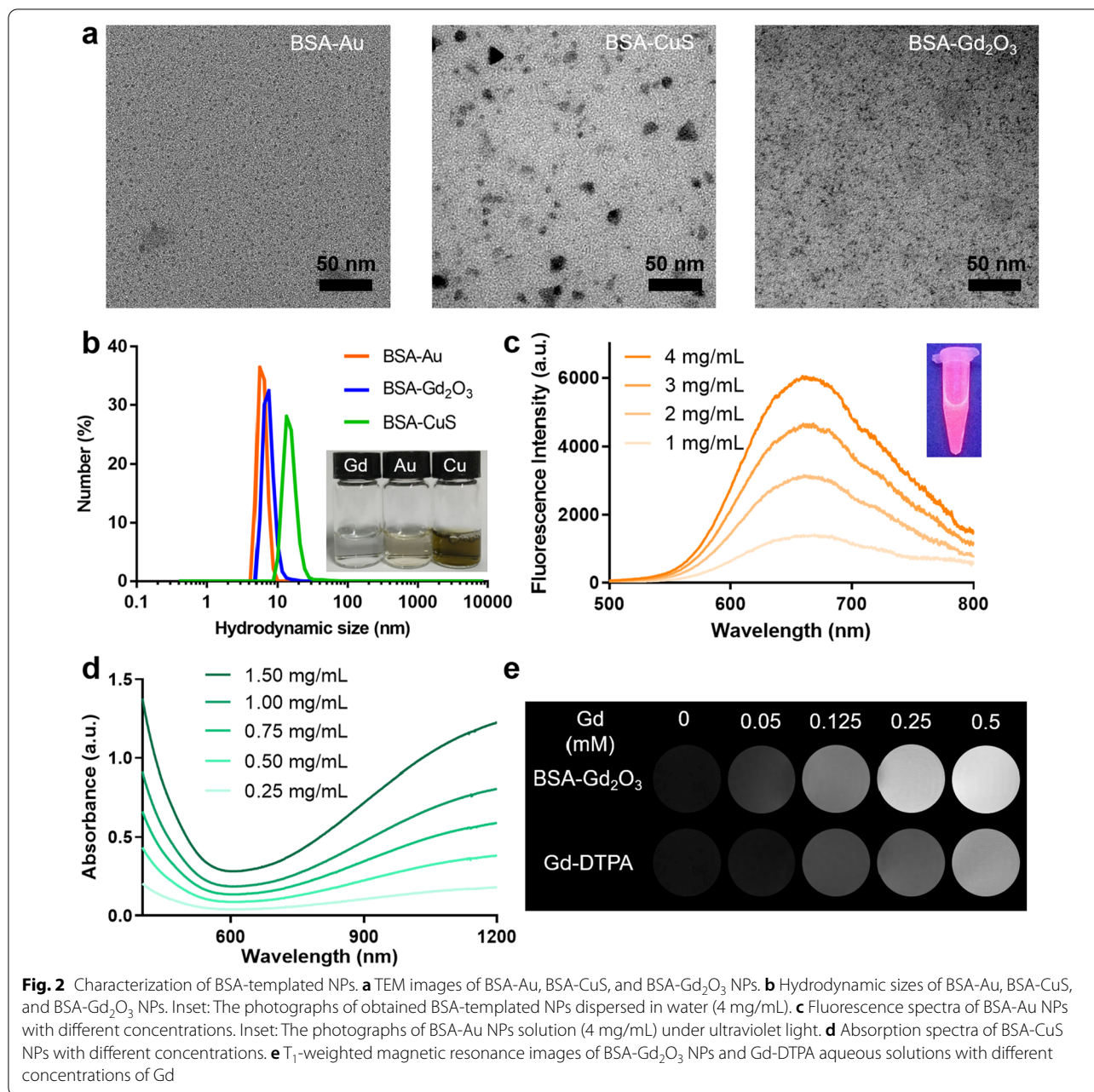
Statistical Analysis

For gene expression, statistical comparisons were performed by using one-way ANOVA as indicated in the figure legends. $P < 0.05$ was considered significant. For GO and KEGG analysis, the Benjamini and Hochberg method for false discovery rate (FDR-BH correction) was applied to correct for multiple comparisons. The number of biological (non-technical) replicates for each experiment was indicated in the figure legends.

Results and Discussion

Synthesis and Characterization of BSA-Templated NPs

Three BSA-templated NPs were synthesized through a classical biomineralization method [53–55], in which BSA as a nanoreactor enables entrapping metal ions based on the interaction between functional groups (e.g., –SH, –NH₂, and –COOH) and metal ions, and controlling the growth of NPs. These NPs showed ultra-small size in both TEM images (~3 nm for BSA-Au NPs, ~3 nm for BSA-Gd₂O₃ NPs, and ~10 nm for BSA-CuS NPs) (Fig. 2a) and hydrodynamic size measurement



(5–20 nm) (Fig. 2b), which is benefited from BSA-directed controlled synthesis. BSA-Au NPs exhibited a strong fluorescent emission peaked at 664 nm (Fig. 2c), which can serve as an excellent fluorescent nanoprobe for biosensing and bioimaging [55]. The d–d transition of Cu²⁺ guarantees the strong near-infrared absorption of BSA-CuS NPs (Fig. 2d), making it a promising photothermal therapy agent for tumor ablation and antimicrobial treatment [53, 56]. BSA-Gd₂O₃ NPs owned a stronger magnetic resonance imaging capability than Gd-DTPA (Fig. 2e), and have been widely used for in vivo

MR imaging [57, 58]. The characteristic FT-IR absorption bands of BSA confirmed the presence of BSA in these NPs (Additional file 1: Fig. S1), and all these NPs showed similar zeta potential with that of BSA solution, indicating BSA serves as the encapsulation layer (Additional file 1: Fig. S2). As shown in Additional file 1: Fig. S3, the appearance of both solid and solution of BSA-templated NPs exhibited no obvious changes, and no precipitate was observed in all solutions. The hydrodynamic sizes of these BSA-templated metallic nanoparticles did not change significantly (Additional file 1: Fig. S4).

Consistently, the optical absorption spectra of BSA-CuS NPs (Additional file 1: Fig. S5), the fluorescence spectra of BSA-Au NPs (Additional file 1: Fig. S6), and the MR signal intensity of BSA-Gd₂O₃ NPs (Additional file 1: Fig. S7) did not change dramatically within 2 weeks no matter in solid or aqueous storage conditions. These results verified the good storage stability of BSA-templated metallic nanoparticles both in solid or aqueous conditions. We also preliminarily evaluated the protein corona formation in vitro by mixing the BSA-templated NPs with 10% FBS under 37 °C and monitoring the hydrodynamic sizes of solutions at different timepoints post-mixing. As shown in Additional file 1: Fig. S8, the hydrodynamic sizes of nanoparticles only and mixed solutions remained relatively stable (approximately 5–20 nm), which did not significantly alter as the incubation time increased. This indicated that BSA-templated NPs did not readily adsorb the proteins probably due to the own albumin template, which is consistent with previous report [59]. Despite the good storage stability and generally accepted biocompatibility of BSA-templated NPs [60–62], the potential effects of biomineralization NPs on the epitranscriptomic changes remain largely unknown.

Global m⁶A Changes in HEK293T Cells Induced by BSA-Templated NPs

In the assessment of cell viability upon the exposure of NPs, neither MTT analysis nor apoptosis assay exhibited obvious cell death when HEK293T cells were incubated with BSA-Au, BSA-CuS and BSA-Gd₂O₃ NPs at the concentrations of 50, 100, and 200 µg/mL (Additional file 1: Figs. S9 and S10). Similarly, no obvious cytotoxicity was observed on 3T3-L1 cells (a mouse embryonic fibroblastic cell line) when incubated with different BSA-templated NPs at different concentrations (Additional file 1: Fig. S11). We also quantitated the uptaken rates of BSA-Au, BSA-Gd₂O₃, and BSA-CuS NPs by HEK293T cells, which were 0.32%, 0.43%, and 2.11%, respectively (Additional file 1: Fig. S12). Then, the m⁶A-seq was performed to explore the NPs-induced RNA methylation changes. As shown in Fig. 3a, b, all the three NPs could induce both upregulated and downregulated m⁶A level. However, the number of genes with downregulated m⁶A level was much greater than that with upregulated m⁶A level, which led to the overall reduced m⁶A landscape. For example, BSA-CuS NPs induced downregulated m⁶A level in 1198 genes, which was far beyond that (156 genes) with upregulated m⁶A level. The genomic landscape of m⁶A distribution indicated that the m⁶A-binding sites of three NPs were similar (Fig. 3c, d). Most of the m⁶A-binding sites were located in protein-coding sequence and are highly enriched for stop codon and 3'UTR, which was consistent with the control group.

Moreover, all the three NPs shared highly conserved m⁶A targets “GGACU” sequence (Fig. 3e), which matched well with the previously reported m⁶A consensus sequence “RRACH” (R=G or A, H=A, C or U) [63]. These findings indicated that BSA-templated NPs could reduce the global m⁶A landscape, but could not affect the distribution of m⁶A and consensus motif. In addition, it has been reported that m⁶A residues can be selectively recognized by the reader protein YTHDF2 to regulate the mRNA degradation [36]. Therefore, the significantly decreased m⁶A level hinted that BSA-templated NPs may own the ability to reprogram epitranscriptome for stability regulation of targeted mRNA.

Functional Annotation of Genes with NPs-Induced m⁶A Changes

Given the important role of m⁶A in various biological processes, the biological functions of genes with NPs-induced m⁶A changes were further investigated by enrichment analysis. As shown in Fig. 4a, b, the cells treated with BSA-Au, BSA-CuS and BSA-Gd₂O₃ NPs displayed both some overlapped peaks (genes with m⁶A) and unique ones no matter with upregulated or downregulated m⁶A level. Considering that different m⁶A peak patterns are related to different cellular functions, functional modeling for genes with upregulated or downregulated m⁶A level under treatment of different BSA-templated NPs was respectively conducted with Kyoto Encyclopedia of Genes and Genomes (KEGG) and gene ontology (GO) analysis. The numbers of genes with downregulated m⁶A were 1062, 1198 and 1249 under treatment of BSA-Au, BSA-CuS and BSA-Gd₂O₃ NPs, respectively. In the KEGG pathway analysis, these genes with downregulated m⁶A level were enriched in multiple pathways, but all pointed to the TGF-beta signaling (Fig. 4c–e). In the annotation of GO, the genes with downregulated m⁶A level were enriched in diverse biological processes, such as RNA metabolic process, nucleic acid process and transcription regulation (Additional file 1: Fig. S13). The differences among BSA-Au, BSA-CuS, and BSA-Gd₂O₃ NPs may be attributed to their distinct physicochemical properties and released metal ions. In spite of this, some common pathways and biological processes could be found among the three NPs-treated HEK293T cells. Particularly, there were 622 common genes with downregulated m⁶A level among the three NPs-treated cells (Fig. 4b). The KEGG analysis of the 622 genes showed that TGF-beta signaling was the most enriched pathway, which was associated with multiple genes like BMP6, SMAD7, CDKN2B, GDF7, and PPP2CB (Fig. 4f). In the meantime, the transcription regulation was the most relevant process as indicated by the GO analysis of the 622 common genes (Fig. 4f).

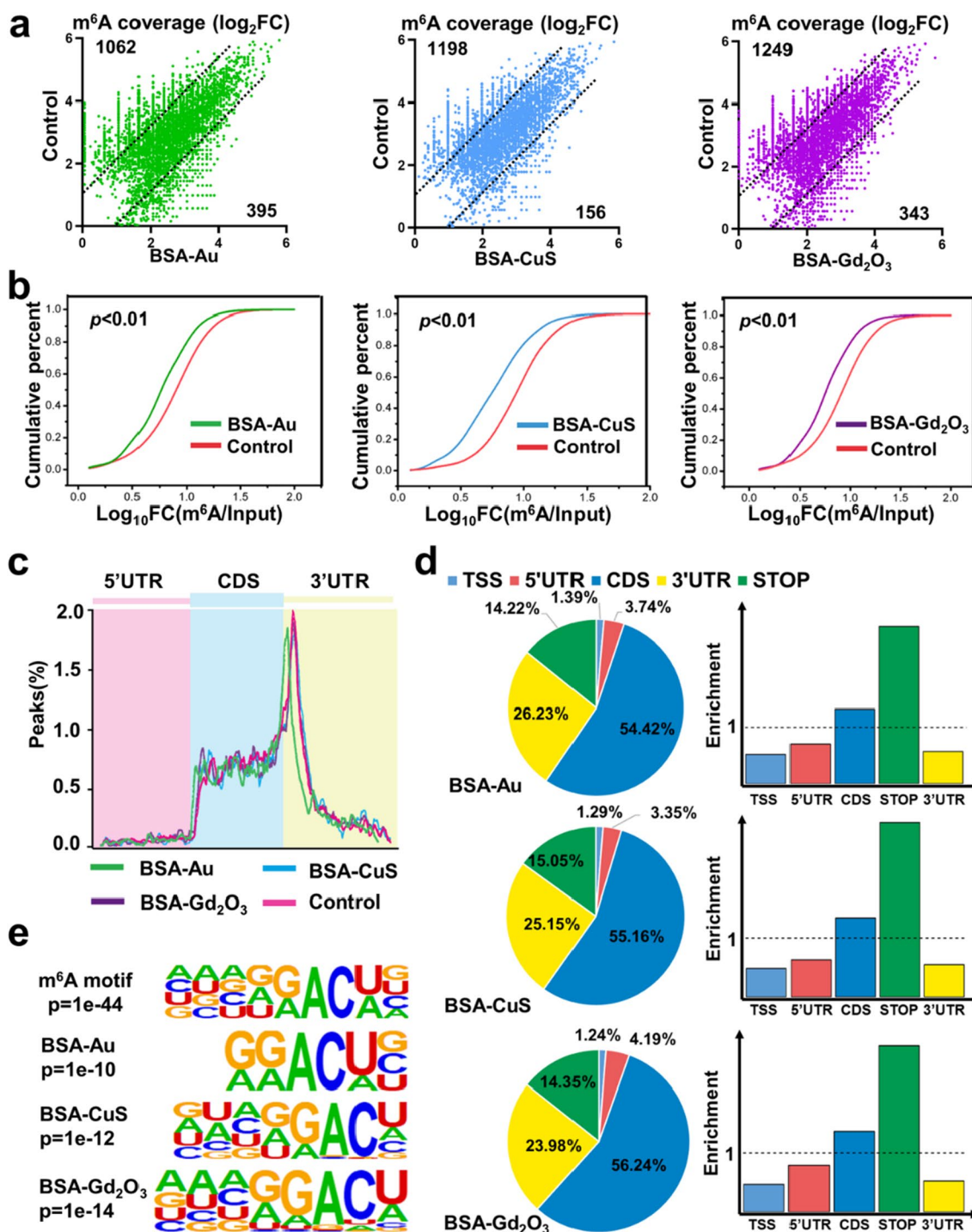


Fig. 3 Global m^6A changes induced by BSA-templated NPs. **a** Scatter plots showing the variation of m^6A coverage of individual m^6A sites in cells treated with BSA-templated NPs. Pair-wise comparison was shown between BSA-Au NPs (left), BSA-CuS NPs (middle), BSA-Gd₂O₃ NPs (right), and controls, respectively. The dashed lines indicated cut-off of \log_2FC (BSA-templated NPs/Control) (1 or -1). The numbers of genes with downregulated ($\log_2FC < -1$) or upregulated ($\log_2FC > 1$) m^6A level was shown. FC, fold change. **b** Cumulative frequency of m^6A targeted genes upon BSA-templated NPs exposure. P values were calculated using two-sided Wilcoxon and Mann-Whitney test. **c** Metagenes profile of enrichment of m^6A -targeted sites across mRNA transcriptome. 5'UTR, 5' untranslated region; CDS, coding sequence; 3'UTR, 3' untranslated region. **d** The distribution (left) and enrichment (right) of m^6A peaks within different gene regions. Enrichment was determined by the proportion of m^6A peaks normalized by the length of the region. **e** Top consensus sequences of m^6A -targeted motif

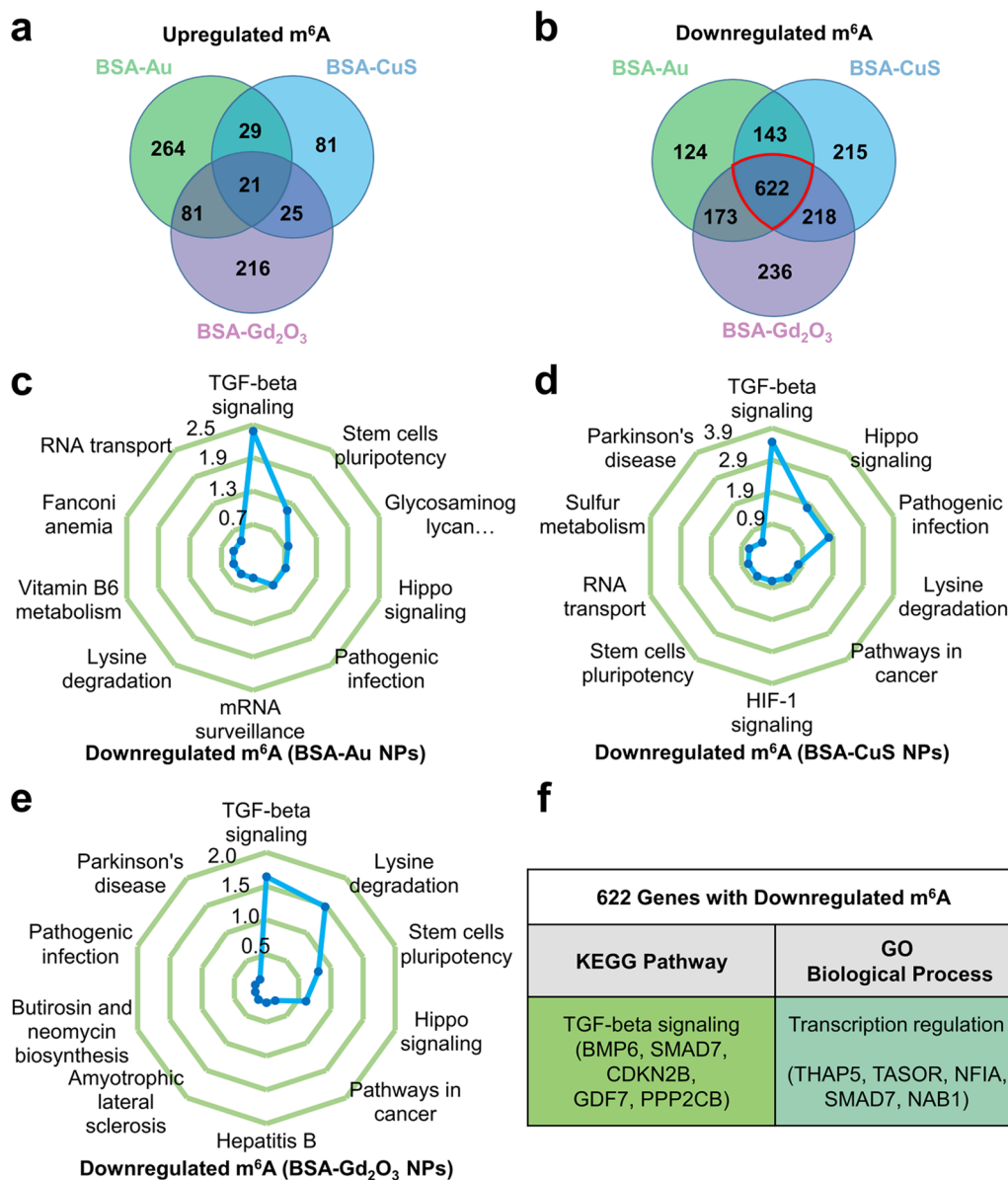


Fig. 4 Functional annotation of the genes with NPs-induced m⁶A changes. **a** Venn diagram of genes with upregulated m⁶A treated with various NPs. **b** Venn diagram of genes with downregulated m⁶A treated with various NPs. **c–e** KEGG pathway analysis of genes with downregulated m⁶A level treated with different NPs. The axis refers to the $-\log_{10}FDR(p)$ value. **f** The most prominent pathway and biological process from the KEGG and GO analysis of three NPs-shared 622 genes with downregulated m⁶A level, respectively

Then, we used MeRIP-qPCR to quantify the m⁶A level of representative genes associated with TGF-beta signaling and transcription regulation process. The results showed that the m⁶A level of BMP6, CDKN2B, GDF7, PPP2CB, TASOR and NAB1 were attenuated by BSA-templated NPs with different patterns (Additional file 1: Figs. S14 and S15), which was consistent with m⁶A-seq results. It is worth mentioning that TGF-beta signaling plays vital roles in a diverse set of cellular processes, such as cell

proliferation, recognition, differentiation, apoptosis, and specification of developmental fate [64]. The KEGG and GO analysis of genes with upregulated m⁶A level induced by the NPs were also displayed (Additional file 1: Figs. S16 and S17). These functional annotations suggested that the genes with m⁶A variations induced by BSA-templated NPs were related to multiple pathways and biological processes, particularly the genes with reduced m⁶A level were enriched for TGF-beta signaling.

Potential Reasons for m⁶A Variations Induced by the NPs

The m⁶A mRNA methylation is regulated and exerts its functions by three groups of “m⁶A RNA modifiers” including m⁶A methyltransferases (writers), m⁶A demethylases (erasers), and m⁶A binding proteins (readers) (Fig. 5a). The writers (e.g., METTL3, METTL14 and WTAP) facilitate the synthesis of m⁶A [65, 66], the erasers (e.g., ALKBH5 and FTO) catalyze the demethylation of m⁶A [67, 68], and the readers (e.g., YTHDC1, YTHDF2 and YTHDF3) specifically recognize m⁶A and regulate its functions, such as splicing and translation [63, 69].

According to the functions of writers, erasers and readers, we hypothesized that the m⁶A alteration induced by BSA-templated NPs was resulted from the dysregulation of the m⁶A-related writers and erasers. To test the hypothesis, we measured gene expression and protein levels of these modifiers in HEK293T cells after being exposed to BSA-templated NPs. As shown in Fig. 5b, c and Additional file 1: S18, these genes did not exhibit a significantly regular expression pattern after exposure to these NPs. This result indicated that the BSA-templated NPs may not induce the m⁶A variations by directly

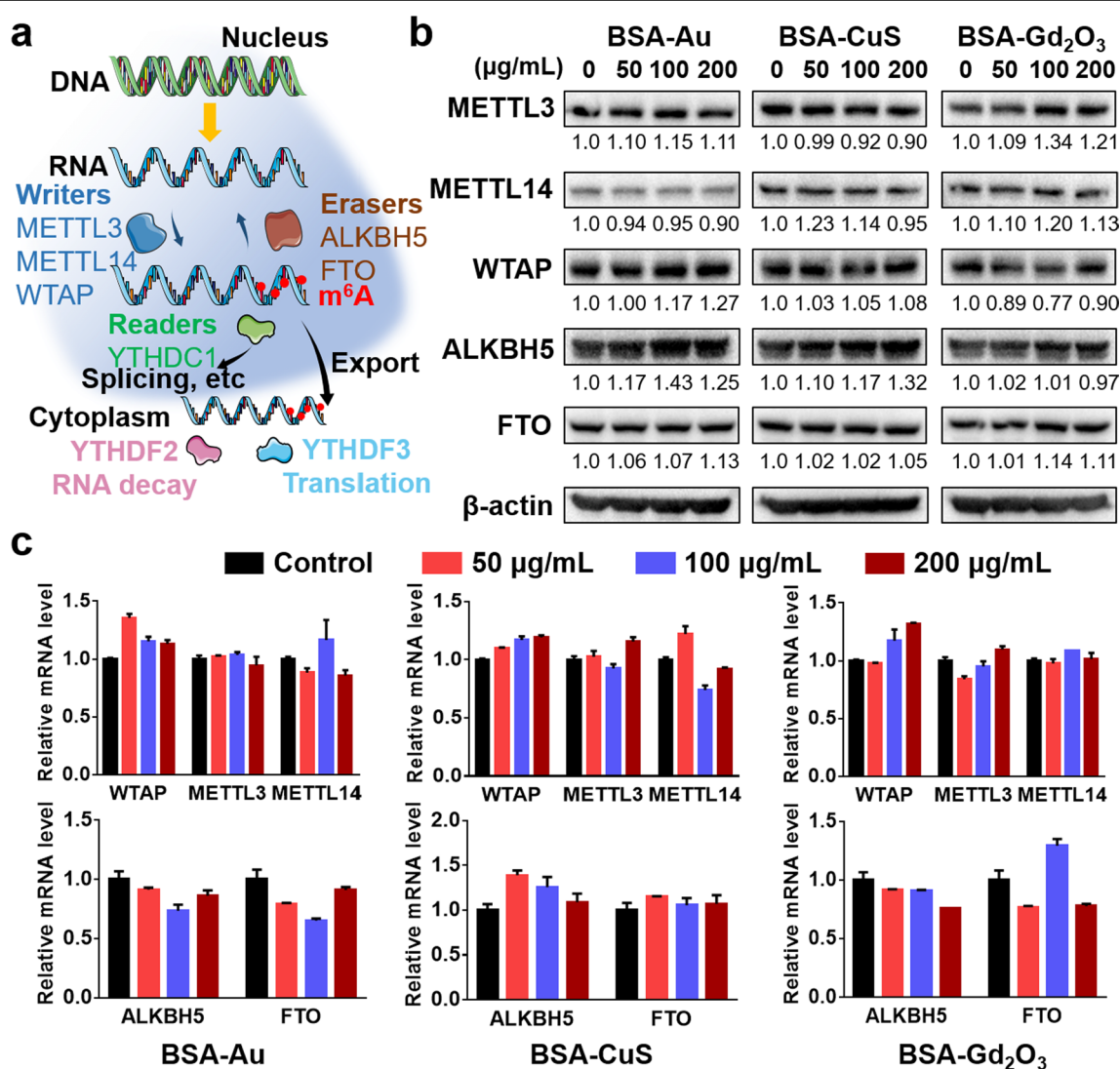


Fig. 5 Expression changes of m⁶A-related writers and erasers upon BSA-templated NPs exposure. **a** Schematic representation of the m⁶A manipulation and function. **b** Western blot analysis of m⁶A-related protein expression in HEK293T cells upon BSA-templated NPs treatment for 24 h. Left panel: exposure to BSA-Au NPs, middle panel: exposure to BSA-CuS NPs, right panel: exposure to BSA-Gd₂O₃ NPs. A total of 30 µg protein was loaded (β-actin was used as a control for loading). **c** Relative mRNA levels of m⁶A-related genes in HEK293T cells upon NPs exposure for 24 h. Left panel: exposure to BSA-Au NPs; middle panel: exposure to BSA-CuS NPs; right panel: exposure to BSA-Gd₂O₃ NPs. Data were shown as the mean ± SD

affecting the expression level of m⁶A-related enzymes, and possible interpretations need to be further explored.

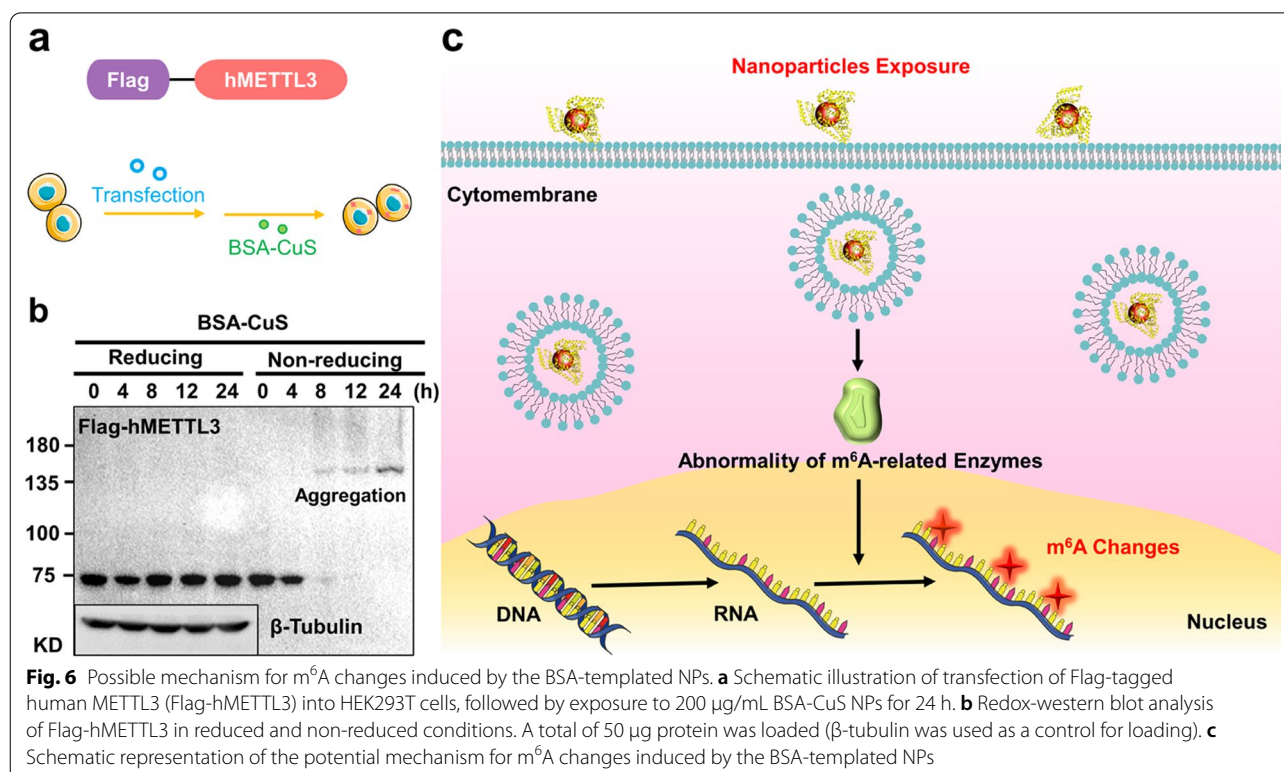
It has been found that glutathione-based nanoclusters can cause Ten-Eleven-Translocation (TET) proteins aggregation, which affects DNA methylation and hydroxyl-methylation [49]. This inspires us to suppose that if NPs could induce abnormal aggregation of m⁶A-related enzymes, leading to the m⁶A distribution reconstruction. To verify the hypothesis, the writer METTL3, one of the earliest discovered m⁶A-related enzymes but with no significant expression change in previous assays [70], was taken into investigation. Flag-tagged METTL3 was transfected into HEK293T cells before exposure to BSA-CuS NPs, which induced the most significant m⁶A change (Fig. 6a). As shown in Fig. 5b, BSA-CuS NPs (200 µg/mL) did not induce significant change in METTL3 expression within 24 h-exposure. Next, to validate if BSA-CuS NPs could affect METTL3, a redox-western blot assay was performed. METTL3 protein complex could be observed under non-reducing condition (Fig. 6b), and more complex formed as incubation time extended. This suggested that BSA-CuS NPs could induce abnormal aggregation of m⁶A writer METTL3. METTL3 is the catalytic subunit in m⁶A methyltransferase complex that transfers a methyl group from S-adenosylmethionine (SAM) to an adenosine in RNA, and the abnormal structure of METTL3 may

directly affect its enzymatic activity for transmethylation. Thus, the aggregation of m⁶A writer METTL3 induced by the NPs may be another underlying mechanism for reprogramming m⁶A enrichment and epitranscriptome.

Based on the above results, despite no obviously detected apoptosis in cells upon exposure of BSA-templated NPs, these NPs could indeed induce the m⁶A changes and potentially affect the cellular biological functions, showing an unprecedented epitranscriptomic scenery induced by NPs. In addition, the potential mechanism for m⁶A changes induced by the BSA-templated NPs has been preliminarily revealed. As shown in Fig. 6c, BSA-templated NPs could result in the abnormality of m⁶A-related enzymes, such as aggregation of m⁶A writers, which at least partly contributed to the alterations of m⁶A landscape.

Conclusions

In this proof-of-concept study, we studied the epitranscriptomic impact (m⁶A) of biomineralization nanoparticles and explored its potential biological mechanisms. We found that BSA-templated NPs could induce epitranscriptomic abnormalities (e.g., reduced m⁶A level), which cannot be detected by conventional biotoxicity assessments. The possible mechanism could be at least partly deduced that the BSA-templated NPs may induce the aggregation of m⁶A-related enzymes



to affect the m⁶A distribution. However, the underlying mechanisms of how NPs affect these m⁶A-related enzymes still need further investigation in the future. Taken together, epitranscriptomics analysis could provide an unprecedented finding of the biological effect induced by NPs, which should be integrated into the nanotoxicity evaluation systems for nanomaterials for their potential clinical translation.

Abbreviations

m⁶A: N⁶-methyladenosine; BSA: Bovine serum albumin; AOP: Adverse outcome pathway; QSAR: Quantitative structure–activity relationship; NPs: Nanoparticles; TEM: Transmission electron microscopy; FT-IR: Fourier transform infrared; MTT: Methyl Thiazolyl Tetrazolium; cDNA: Complementary DNA.

Supplementary Information

The online version contains supplementary material available at <https://doi.org/10.1186/s11671-022-03663-x>.

Additional file 1. Sequences of PCR primers; FT-IR spectra, Zeta potential, hydrodynamic sizes, absorption spectra, fluorescence spectra, and magnetic resonance imaging of NPs; cell viabilities; cellular uptake rates of NPs; GO and KEGG analysis; PCR analysis, and Western blot analysis.

Acknowledgements

Thanks to all the peer reviewers and editors for their opinions and suggestions.

Authors' Contributions

JP and JZ designed the study. JZ and JW performed experiments and analyzed the data. KF and XM supervised the data collection. WH and BL interpreted the data. JP and JZ prepared the manuscript for publication and reviewed the draft of the manuscript. All authors have read and approved the manuscript.

Funding

This work was supported by the National Natural Science Foundation of China (81801829, 81572154, 81871777, 82102639), Natural Science Foundation of Tianjin (18JCQNJC14300, 20JCQNJC01170), and the Science & Technology Development Fund of Tianjin Education Commission for Higher Education (2017KJ192) and Tianjin Health Science and Technology Project (TJWJ2021QN047).

Availability of Data and Materials

All data supporting the conclusions of this article are included within the article.

Declarations

Competing interest

The authors declare that they have no competing interests.

Author details

¹Department of Radiology, Tianjin Key Laboratory of Functional Imaging, Tianjin Medical University General Hospital, Tianjin 300052, China. ²Department of Orthopedics, Tianjin Hospital, Tianjin University, Tianjin 300211, China. ³Department of Radiology, The Second Hospital of Tianjin Medical University, Tianjin 300211, China. ⁴Department of Radiology, Beijing Chest Hospital, Capital Medical University, Beijing Tuberculosis and Thoracic Tumor Research Institute, Beijing 101149, China. ⁵Department of Diagnostic and Therapeutic Ultrasonography, Tianjin Medical University Cancer Institute and Hospital, National Clinical Research Center of Cancer, Key Laboratory of Cancer Prevention and Therapy, Tianjin's Clinical Research Center for Cancer, Tianjin 300060, China.

Received: 8 October 2021 Accepted: 26 January 2022

Published online: 05 February 2022

References

- Soenen SJ, Parak WJ, Rejman J, Manshian B (2015) (Intra)Cellular stability of inorganic nanoparticles: effects on cytotoxicity, particle functionality, and biomedical applications. *Chem Rev* 115:2109–2135
- Sharifi S, Behzadi S, Laurent S, Forrest ML, Stroeve P, Mahmoudi M (2012) Toxicity of nanomaterials. *Chem Soc Rev* 41:2323–2343
- Min Y, Caster JM, Eblan MJ, Wang AZ (2015) Clinical translation of nanomedicine. *Chem Rev* 115:11147–11190
- Hofmann-Antenbrink M, Grainger DW, Hofmann H (2015) Nanoparticles in medicine: current challenges facing inorganic nanoparticle toxicity assessments and standardizations. *Nanomedicine* 11:1689–1694
- Nystrom AM, Fadeel B (2012) Safety assessment of nanomaterials: Implications for nanomedicine. *J Control Release* 161:403–408
- Scott-Fordsmand JJ, Pozzi-Mucelli S, Tran L, Aschberger K, Sabella S, Vogel U et al (2014) A unified framework for nanosafety is needed. *Nano Today* 9:546–549
- Chen R, Qiao J, Bai R, Zhao Y, Chen C (2018) Intelligent testing strategy and analytical techniques for the safety assessment of nanomaterials. *Anal Bioanal Chem* 410:6051–6066
- Fadeel B, Farcal L, Hardy B, Vazquez-Campos S, Hristozov D, Marcomini A et al (2018) Advanced tools for the safety assessment of nanomaterials. *Nat Nanotech* 13:537–543
- Kanakis S, Toussaint JD, Chowdhury SM, Tembulkar T, Lee S, Jiang Y-P et al (2014) Dose ranging, expanded acute toxicity and safety pharmacology studies for intravenously administered functionalized graphene nanoparticle formulations. *Biomaterials* 35:7022–7031
- Hall S, Bradley T, Moore JT, Kuykindall T, Minella L (2009) Acute and chronic toxicity of nano-scale TiO₂ particles to freshwater fish, cladocerans, and green algae, and effects of organic and inorganic substrate on TiO₂ toxicity. *Nanotoxicology* 3:91–97
- Ruiz A, Ali LMA, Caceres-Velez PR, Cornudella R, Gutierrez M, Moreno JA et al (2015) Hematotoxicity of magnetite nanoparticles coated with polyethylene glycol: in vitro and in vivo studies. *Toxicol Res* 4:1555–1564
- Ema M, Kobayashi N, Naya M, Hanai S, Nakanishi J (2010) Reproductive and developmental toxicity studies of manufactured nanomaterials. *Reprod Toxicol* 30:343–352
- Dobrovolskaia MA, Germolec DR, Weaver JL (2009) Evaluation of nanoparticle immunotoxicity. *Nat Nanotech* 4:411–414
- Chen R, Huo L, Shi X, Bai R, Zhang Z, Zhao Y et al (2014) Endoplasmic reticulum stress induced by zinc oxide nanoparticles is an earlier biomarker for nanotoxicological evaluation. *ACS Nano* 8:2562–2574
- Kao Y-Y, Chen Y-C, Cheng T-J, Chiung Y-M, Liu P-S (2012) Zinc oxide nanoparticles interfere with zinc ion homeostasis to cause cytotoxicity. *Toxicol Sci* 125:462–472
- Andon FT, Fadeel B (2013) Programmed cell death: molecular mechanisms and implications for safety assessment of nanomaterials. *Acc Chem Res* 46:733–742
- Singh N, Manshian B, Jenkins GJS, Griffiths SM, Williams PM, Maffei TGG et al (2009) NanoGenotoxicology: the DNA damaging potential of engineered nanomaterials. *Biomaterials* 30:3891–3914
- Toyokuni S (2013) Genotoxicity and carcinogenicity risk of carbon nanotubes. *Adv Drug Deliver Rev* 65:2098–2110
- Vinken M (2013) The adverse outcome pathway concept: a pragmatic tool in toxicology. *Toxicology* 312:158–165
- Puzyn T, Jeliakova N, Sarimveis H, Robinson RLM, Lobaskin V, Rallo R et al (2018) Perspectives from the nanosafety modelling cluster on the validation criteria for (Q)SAR models used in nanotechnology. *Food Chem Toxicol* 112:478–494
- Puzyn T, Rasulev B, Gajewicz A, Hu X, Dasari TP, Michalkova A et al (2011) Using nano-QSAR to predict the cytotoxicity of metal oxide nanoparticles. *Nat Nanotech* 6:175–178
- Shin TH, Lee DY, Lee H-S, Park HJ, Jin MS, Paik M-J et al (2018) Integration of metabolomics and transcriptomics in nanotoxicity studies. *BMB Rep* 51:14–20
- Revel M, Chatel A, Mouneyrac C (2017) Omics tools: New challenges in aquatic nanotoxicology? *Aquat Toxicol* 193:72–85

24. Lee T-L, Chan W-Y, Rennert OM (2009) Assessing the safety of nanomaterials by genomic approach could be another alternative. *ACS Nano* 3:3830–3830
25. Chen Y, Xu M, Zhang J, Ma J, Gao M, Zhang Z et al (2017) Genome-wide DNA methylation variations upon exposure to engineered nanomaterials and their implications in nanosafety assessment. *Adv Mater* 29:1604580
26. Kinaret P, Marwah V, Fortino V, Ilves M, Wolff H, Ruokolainen L et al (2017) Network analysis reveals similar transcriptomic. Responses to intrinsic properties of carbon nanomaterials in vitro and in vivo. *ACS Nano* 11:3786–3796
27. Du C, Zhang B, He Y, Hu C, Ng QX, Zhang H et al (2017) Biological effect of aqueous C-60 aggregates on *Scenedesmus obliquus* revealed by transcriptomics and non-targeted metabolomics. *J Hazard Mater* 324:221–229
28. Matysiak M, Kapka-Skrzypczak L, Brzoska K, Gutleb AC, Kruszewski M (2016) Proteomic approach to nanotoxicity. *J Proteomics* 137:35–44
29. Soria NGC, Aga DS, Atilla-Gokcumen GE (2019) Lipidomics reveals insights on the biological effects of copper oxide nanoparticles in a human colon carcinoma cell line. *Mol Omics* 15:30–38
30. Lee S-H, Tang C-H, Lin W-Y, Chen K-H, Liang H-J, Cheng T-J et al (2018) LC-MS-based lipidomics to examine acute rat pulmonary responses after nano- and fine-sized ZnO particle inhalation exposure. *Nanotoxicology* 12:439–452
31. Lv M, Huang W, Chen Z, Jiang H, Chen J, Tian Y et al (2015) Metabolomics techniques for nanotoxicity investigations. *Bioanalysis* 7:1527–1544
32. Boyles MSP, Ranninger C, Reischl R, Rurik M, Tessadri R, Kohlbacher O et al (2016) Copper oxide nanoparticle toxicity profiling using untargeted metabolomics. *Part Fibre Toxicol* 13:49
33. Li XY, Xiong XS, Yi CQ (2017) Epitranscriptome sequencing technologies: decoding RNA modifications. *Nat Methods* 14:23–31
34. Deng X, Su R, Weng H, Huang H, Li Z, Chen J (2018) RNA N(6)-methyladenosine modification in cancers: current status and perspectives. *Cell Res* 28:507–517
35. Liu N, Dai Q, Zheng G, He C, Parisien M, Pan T (2015) N-6-methyladenosine-dependent RNA structural switches regulate RNA-protein interactions. *Nature* 518:560–564
36. Wang X, Lu Z, Gomez A, Hon GC, Yue Y, Han D et al (2014) N6-methyladenosine-dependent regulation of messenger RNA stability. *Nature* 505:117–120
37. Meyer KD, Jaffrey SR (2014) The dynamic epitranscriptome: N-6-methyladenosine and gene expression control. *Nat Rev Mol Cell Bio* 15:313–326
38. Zhang CX, Chen YS, Sun BF, Wang L, Yang Y, Ma DY et al (2017) m(6)A modulates haematopoietic stem and progenitor cell specification. *Nature* 549:273–276
39. Huang HL, Weng HY, Chen JJ (2020) The biogenesis and precise control of RNA m(6)A methylation. *Trends Genet* 36:44–52
40. Ma JZ, Yang F, Zhou CC, Liu F, Yuan JH, Wang F et al (2017) METTL14 suppresses the metastatic potential of hepatocellular carcinoma by modulating N(6)-methyladenosine-dependent primary MicroRNA processing. *Hepatology* 65:529–543
41. Min KW, Zealy RW, Davila S, Fomin M, Cummings JC, Makowsky D et al (2018) Profiling of m6A RNA modifications identified an age-associated regulation of AGO2 mRNA stability. *Aging Cell* e12753
42. Yang Y, Hsu PJ, Chen YS, Yang YG (2018) Dynamic transcriptomic m(6)A decoration: writers, erasers, readers and functions in RNA metabolism. *Cell Res* 28:616–624
43. Su R, Dong L, Li C, Nachtergaele S, Wunderlich M, Qing Y et al (2018) R-2HG Exhibits Anti-tumor Activity by Targeting FTO/m(6)A/MYC/CEBPA Signaling. *Cell* 172:90–105
44. Ruan F, Zeng J, Yin H, Jiang S, Cao X, Zheng N et al (2021) RNA m6A modification alteration by black phosphorus quantum dots regulates cell ferroptosis: implications for nanotoxicological assessment. *Small Methods* 5:2001045
45. Chen Q, Liu Z (2016) Albumin carriers for cancer theranostics: a conventional platform with new promise. *Adv Mater* 28:10557–10566
46. Zan G, Wu Q (2016) Biomimetic and bioinspired synthesis of nanomaterials/nanostructures. *Adv Mater* 28:2099–2147
47. Dominissini D, Moshitch-Moshkovitz S, Salmon-Divon M, Amariglio N, Rechavi G (2013) m6A-seq: transcriptome-wide mapping of N(6)-methyladenosine by m(6)A-seq based on immunocapturing and massively parallel sequencing. *Nat Protoc* 8:176–189
48. Robinson JT, Thorvaldsdottir H, Winckler W, Guttman M, Lander ES, Getz G et al (2011) Integrative genomics viewer. *Nat Biotechnol* 29:24–26
49. Ma Y, Fu H, Zhang C, Cheng S, Gao J, Wang Z et al (2016) Chiral antioxidant-based gold nanoclusters reprogram DNA epigenetic patterns. *Sci Rep* 6:33436
50. Zhao J, Ma XL, Ma JX, Sun L, Lu B, Wang Y et al (2017) TET3 mediates alterations in the epigenetic marker 5hmC and Akt pathway in steroid-associated osteonecrosis. *J Bone Miner Res* 32:319–332
51. Li B, Zhao J, Ma J, Chen W, Zhou C, Wei W et al (2021) Cross-talk between histone and DNA methylation mediates bone loss in hind limb unloading. *J Bone Miner Res* 36:956–967
52. Zhao J, Li B, Ma J, Jin W, Ma X (2020) Photoactivatable RNA N(6)-methyladenosine editing with CRISPR-Cas13. *Small* 16:e1907301
53. Zhang C, Fu Y-Y, Zhang X, Yu C, Zhao Y, Sun S-K (2015) BSA-directed synthesis of CuS nanoparticles as a biocompatible photothermal agent for tumor ablation in vivo. *Dalton Trans* 44:13112–13118
54. Zhang BB, Jin HT, Li Y, Chen BD, Liu SY, Shi DL (2012) Bioinspired synthesis of gadolinium-based hybrid nanoparticles as MRI blood pool contrast agents with high relaxivity. *J Mater Chem* 22:14494–14501
55. Xie JP, Zheng YG, Ying JY (2009) Protein-directed synthesis of highly fluorescent gold nanoclusters. *J Am Chem Soc* 131:888–889
56. Yang WT, Guo WS, Le WJ, Lv GX, Zhang FH, Shi L et al (2016) Albumin-bioinspired Gd:CuS nanotheranostic agent for in vivo photoacoustic/magnetic resonance imaging-guided tumor-targeted photothermal therapy. *ACS Nano* 10:10245–10257
57. Sun S-K, Dong L-X, Cao Y, Sun H-R, Yan X-P (2013) Fabrication of multifunctional Gd₂O₃/Au hybrid nanoprobe via a one-step approach for near-infrared fluorescence and magnetic resonance multimodal imaging in vivo. *Anal Chem* 85:8436–8441
58. Wang Y, Yang T, Ke H, Zhu A, Wang Y, Wang J et al (2015) Smart Albumin-biomaterialized nanocomposites for multimodal imaging and photothermal tumor ablation. *Adv Mater* 27:3874–3882
59. Peng Q, Zhang S, Yang Q, Zhang T, Wei XQ, Jiang L et al (2013) Preformed albumin corona, a protective coating for nanoparticles based drug delivery system. *Biomaterials* 34:8521–8530
60. Elzoghby AO, Samy WM, Elgindy NA (2012) Albumin-based nanoparticles as potential controlled release drug delivery systems. *J Control Release* 157:168–182
61. Wang J, Zhang BB (2018) Bovine serum albumin as a versatile platform for cancer imaging and therapy. *Curr Med Chem* 25:2938–2953
62. Liu XW, Wang C, Liu Z (2018) Protein-engineered biomaterials for cancer theranostics. *Adv Healthc Mater* 7:e1800913
63. Patil DP, Pickering BF, Jaffrey SR (2018) Reading m(6)A in the transcriptome: m(6)A-binding proteins. *Trends Cell Biol* 28:113–127
64. Shi YG, Massague J (2003) Mechanisms of TGF-beta signaling from cell membrane to the nucleus. *Cell* 113:685–700
65. Liu J, Yue Y, Han D, Wang X, Fu Y, Zhang L et al (2014) A METTL3-METTL14 complex mediates mammalian nuclear RNA N6-adenosine methylation. *Nat Chem Biol* 10:93–95
66. Yue Y, Liu J, Cui X, Cao J, Luo G, Zhang Z et al (2018) VIRMA mediates preferential m(6)A mRNA methylation in 3'UTR and near stop codon and associates with alternative polyadenylation. *Cell Discov* 4:10
67. Zheng G, Dahl JA, Niu Y, Fedorcsak P, Huang CM, Li CJ et al (2013) ALKBH5 is a mammalian RNA demethylase that impacts RNA metabolism and mouse fertility. *Mol Cell* 49:18–29
68. Yu J, Chen M, Huang H, Zhu J, Song H, Park J et al (2018) Dynamic m6A modification regulates local translation of mRNA in axons. *Nucleic Acids Res* 46:1412–1423
69. Meyer KD, Patil DP, Zhou J, Zinoviev A, Skabkin MA, Elemento O et al (2015) 5' UTR m(6)A promotes cap-independent translation. *Cell* 163:999–1010
70. Liu JZ, Yue YN, Han DL, Wang X, Fu Y, Zhang L et al (2014) A METTL3-METTL14 complex mediates mammalian nuclear RNA N6-adenosine methylation. *Nat Chem Biol* 10:93–95

Publisher's Note

Springer Nature remains neutral with regard to jurisdictional claims in published maps and institutional affiliations.